ELSEVIER

Journal of Structural Geology 30 (2008) 21–28

JOURNAL OF STRUCTURAL GEOLOGY

www.elsevier.com/locate/jsg

Along-strike variations of the slip direction on normal faults: Insights from three-dimensional finite-element models

Georgios Maniatis*, Andrea Hampel

Institut für Geologie, Mineralogie und Geophysik, Ruhr-Universität Bochum, Universitätsstrasse 150, 44801 Bochum, Germany

Received 2 July 2007; received in revised form 16 October 2007; accepted 22 October 2007
Available online 5 November 2007

Abstract

Normal faults in nature exhibit a systematic variation of the slip direction along strike, with pure dip-slip at their centres that changes gradually to oblique slip near their tips. Here we evaluate the variation of the slip direction along normal faults by three-dimensional finite-element modelling. The model results reveal a nearly linear increase of the strike-slip component over two-thirds of the distance from the fault centre to its tips, which results in an increasing obliqueness of the slip vector along strike. Excluding the fault tips, the relationship between lateral slip and fault length can be approximated by a power-law function, which shows that the strike-slip component is proportional to the dip-slip and to the fault dip. The development of the sinistral and dextral slip components is caused by the orientation of the minimum principal stress, which is deflected toward the fault centre in both footwall and hanging wall. A comparison with two faults in the Central Apennines, Italy, shows good agreement between modelled and measured slip vectors. The occurrence of converging slip patterns implies that caution is advised when inferring oblique extension, regional stress trajectories and palaeostress fields from slip vectors measured away from the fault centre.

Keywords: Normal faults; Finite-element models; Slip direction; Stress field

1. Introduction

Studies of kinematic indicators on fault planes have revealed that the slip direction varies systematically along normal faults (e.g. Jackson et al., 1982; Roberts, 1996; Roberts and Ganas, 2000; Roberts and Michetti, 2004; Michetti et al., 2000). At the centres of normal faults oriented perpendicular to the regional extension direction almost pure dip-slip motion occurs, whereas near the fault tips substantial oblique slip toward the centre of the hanging wall is observed (Fig. 1a). This variation in slip direction can be expressed in terms of the rake α (Fig. 1b). Well-documented examples of up to 40-km long normal faults exhibiting converging slip vectors have been reported from the Lazio-Abruzzo Apennines in central Italy (Roberts and Michetti, 2004), from southern Italy (Roberts, 2007) and from the gulfs of Corinth and Evia in central Greece (Roberts, 1996; Roberts and Koukouvelas, 1996; Roberts and Ganas, 2000). Along-strike variations of the slip direction have further been observed on the normal fault that ruptured during the 1983 Borah Peak, Idaho, earthquake (Crone et al., 1987; Roberts, 2007) and on non-parallel faults in central Utah (Maerten, 2000).

The converging slip pattern has been attributed to along-strike extension within the hanging wall (Jackson et al., 1982). More precisely, the hanging wall of normal faults is stretched along strike because hanging wall subsidence is greater than footwall uplift and fault throw is greatest at fault centres whereas it decreases to zero at the fault tips (Ma and Kusznir, 1995; Wu and Bruhn, 1994). The latter phenomenon is responsible for a large component of strike-slip motion and oblique slip vectors near the fault tips (Morewood and Roberts, 1997; Roberts, 1996).

While the relationship between the amount of dip-slip on normal faults and fault length has been studied by numerical modelling (e.g. Willemse et al., 1996; Cowie, 1998), the evolution of the strike-slip component has hitherto not been

* Corresponding author. Tel.: +49 (0)234 32 23230; fax: +49 (0)234 32 14572.
E-mail address: georgios.maniatis@rub.de (G. Maniatis).

0191-8141/$ - see front matter © 2007 Elsevier Ltd. All rights reserved.
doi:10.1016/j.jsg.2007.10.002

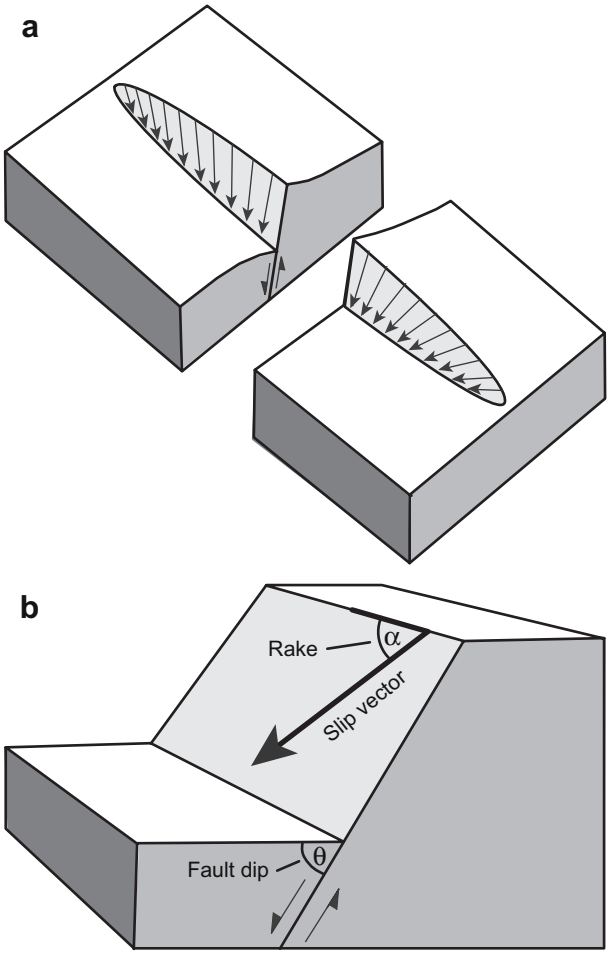

Fig. 1. (a) Sketch of a normal fault with a converging slip pattern. With increasing distance from the fault centre, the slip direction becomes oblique (modified from Roberts and Ganas, 2000). (b) The acute angle between fault strike and the slip vector on the fault plane is termed rake α. The dip angle of the fault is θ.

addressed in a quantitative way. Here we apply three-dimensional numerical models including a normal fault to investigate how geometrical factors such as fault length, dip angle, throw, and distance from the fault centre influence the magnitude of the strike-slip component and the slip direction along the fault. Based on the model results, we derive simple mathematical expressions how the strike-slip and dip-slip components are related to the fault geometry. Furthermore, we analyse the stress field near the model fault to shed light on the underlying causes of the converging slip pattern. Finally, we compare our experimental results with data from faults in Italy.

2. Model setup

Our finite-element models, which were created using the commercial software ABAQUS (Hibbitt et al., 2006), consist of a 500 km × 500 km large lithosphere with a total thickness of 100 km (Fig. 2). The lithosphere is divided into an elastic upper crust, a viscoelastic lower crust and a viscoelastic lithospheric mantle. Details on the geometry and the rheological parameters are given in Fig. 2. Gravity is applied as a body force and isostasy is simulated by applying a lithostatic pressure and linear spring and dashpot elements at the bottom of the models. The combination of dashpot and spring elements accounts for an asthenosphere with a density of $\rho = 3200\ \mathrm{kg/m^3}$ and a viscosity of $\eta = 1 \times 10^{18}$ Pa s, which is within the range of values determined from lithospheric flexure and isostatic rebound of northern Europe and North America (Bills et al., 1994; Fjeldskaar, 1994; Lambeck et al., 1998; Kaufmann and Amelung, 2000).

In the centre of the model, a rectangular fault is embedded in the upper crust and extends to the top of the lower crust at 15 km depth in all experiments (Fig. 2). The down-dip size of the fault depends on the fault dip; for example, it is 17.3 km for a 60°-dipping fault. Fault dip and length vary between different experiments but they do not change within an experiment, i.e. the faults are not allowed to propagate. By using this approach, we follow the growth model proposed by Walsh et al. (2002) who suggest that fault lengths are nearly constant from an early stage and growth is achieved mainly by increase in cumulative displacement. Slip on the fault is controlled by the Mohr–Coulomb failure criterion:

$$\tau = c + \mu\sigma_{\mathrm{n}} \tag{1}$$

where τ is the shear strength along the fault plane, c is the cohesion, μ is the friction coefficient and $\sigma_{\mathbf{n}}$ is the normal stress on the fault plane. In our experiments, the friction coefficient is $\mu = 0.4$, whereas the cohesion is zero because fault rocks have negligible cohesion (e.g. Twiss and Moores, 1992). The use of the Mohr–Coulomb criterion implies that the intermediate principal stress σ_2 is not taken into account when determining the state of stress on the fault.

All experiments start with the establishment of isostatic equilibrium. Afterwards, the lithosphere is extended by imposing a horizontal velocity of 5 mm/a on both sides that are parallel to the strike of the fault (Fig. 2). Horizontal extension of the model initiates normal slip on the fault, which attains a steady-state slip rate within the first 150 ka. All experiments are run until the fault has achieved a displacement–length ratio in accordance with the fault scaling law (Cowie and Scholz, 1992a,b,c; Schlische et al., 1996):

$$D = 0.03L^{1.06} \tag{2}$$

where D is the displacement at the fault centre (in metres) and L is the fault length (in metres). In this way we ensure that each model fault reaches a plausible amount of cumulative throw that is consistent with existing displacement–length data (e.g. Walsh and Watterson, 1988; Schlische et al., 1996; Kim and Sanderson, 2005).

3. Model results

We carried out a total of 18 experiments, with fault dips of 30°, 45° and 60° and fault lengths that varied between 5 km and 40 km (Table 1). As the extension rate is the same in all

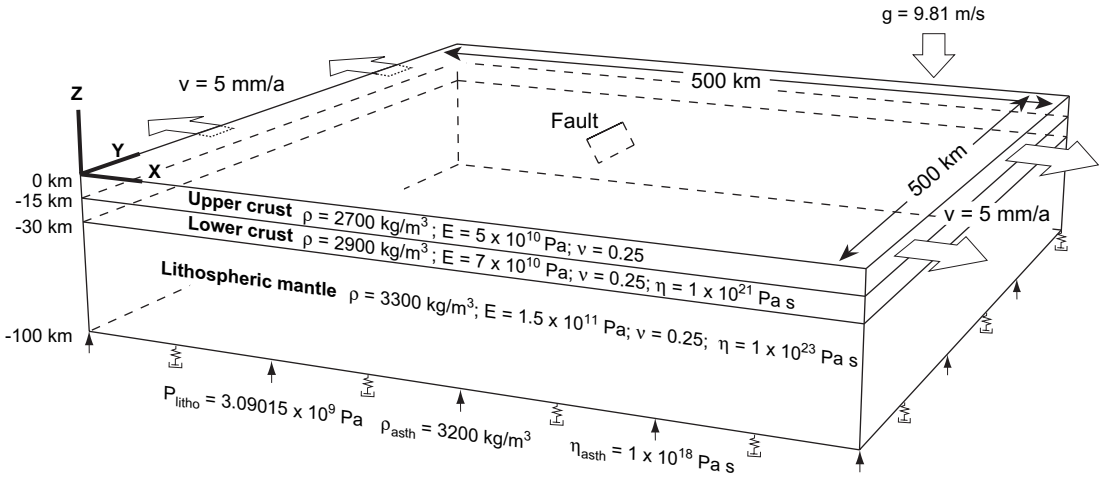

Fig. 2. Perspective view of the three-dimensional finite-element model. A fault incorporated in the centre of the upper crust develops as a normal fault as the model lithosphere is extended at a rate of 5 mm/a. Extension is achieved by applying a velocity boundary condition to the models sides that are parallel to the fault's strike. The dip and length of the fault are systematically varied in a suite of experiments. As the fault extends to the base of the upper crust (located at a depth of 15 km), its down-dip length depends on the fault dip. Note that during each experiment the fault length, dip and down-dip length are constant. Isostasy is included by applying a lithostatic pressure and linear spring and dashpot elements at the bottom of the model. Other parameters are: ρ, density; E, elastic modulus; ν, Poisson's ratio; η, viscosity; g, acceleration due to gravity.

models, the total model time until the fault has reached a displacement–length ratio of 0.03 according to the fault scaling law increases with fault length (Table 1). The slip accumulated on the fault is not equal to the amount of horizontal extension because part of the extension is taken up by elastic and viscoelastic strain of the surrounding model layers.

Fig. 3 shows that the dip-slip displacement is largest in the centre of the fault and decreases to zero toward its tips in all experiments. The resulting displacement profiles are arc-shaped, as expected for non-propagating faults embedded in an elastic and homogenous medium (cf. Cowie and Scholz, 1992b; Manighetti et al., 2001). Regardless of fault dip or length, a significant strike-slip component develops in all experiments, which reaches a maximum close to the fault tips (Fig. 3b). The distance between the fault centre, where pure dip-slip occurs, and the location of maximum strike-slip movement is always about three-quarters of the fault half-length. Beyond that maximum, the lateral slip decreases non-linearly to zero at the pinned fault tips. The direction of hanging-wall movement is always toward the fault centre, i.e. the sense of strike-slip motion is dextral in one half of the fault and sinistral in the other half of the fault (Fig. 3b). The obliqueness of the slip direction increases from the fault centre toward its tips owing to the changing ratio between dip-slip and lateral slip. As a result, the rake α (Fig. 1b), decreases from 90° at the fault centre to ~60° near the fault tips (Fig. 3c).

In the following we evaluate how the fault length and geometry affect the distribution of dip-slip, lateral slip and slip direction on the modelled normal faults. Fig. 4 shows a comparison between five faults with the same dip angles and same amount of dip-slip at their centres (521 m) but with lengths ranging from 10 km to 40 km, respectively. Shorter faults have lateral-slip distributions with steeper gradients, i.e. at the same distance away from the fault centre the amount of lateral slip is greater. However, the maximum amount of lateral slip occurring on the five faults is similar. As a consequence, the slip vectors at the same distance away from the fault centre are more oblique on shorter faults (Fig. 4c).

The influence of the fault dip angle on the slip pattern along the faults is shown in Fig. 5 for three 10-km long faults with dip angles of 30°, 45° and 60° respectively. The amount of dip-slip at the fault centre is the same and the dip-slip distribution is identical regardless of the dip angle (Fig. 5). The strike-slip distributions show clearly that the shallow dipping faults accumulate more lateral slip along their lengths and consequently their slip vectors are more oblique (Fig. 5b,c). Another important characteristic of all modelled faults is that the rake α remains approximately the same at any point along a fault, i.e. the rake does not depend on the amount of dip-slip at the fault centre (Fig. 6).

4. Quantitative relationships between fault geometry and the dip-slip and strike-slip components

Our model results show that the strike-slip and dip-slip components as well as the rake vary systematically along all model faults. In the following, we derive two mathematical expressions that describe the relationship between the dip-slip, lateral slip, rake and the geometry of a fault that derive from our set of experiments (Table 1).

The first function relates the amount of strike-slip to the amount of dip-slip at the fault centre, fault length and dip angle. Note that we focus on the near-linear part of the strike-slip curves between the fault centre and the lateral slip maximum (Fig. 3) to set up Eq. (3). The regression of the strike-slip curves from all modelled faults shows that the amount of strike-slip along a normal fault is directly proportional to the

Table 1
Results of the 18 experiments

Fault length (km)	5			10			15			20			30			40		
Dip angle (°)	30	45	60	30	45	60	30	45	60	30	45	60	30	45	60	30	45	60
Dip-slip at fault centre (m)		250			521			801			1087			1671			2266	
Maximum strike-slip (m)[a]	67	54	43	436	110	87	207	168	134	257	206	170	400	321	259	520	420	331
Model time (Myr)[b]	1.69	1.66	1.72	1.74	1.64	1.76	1.80	1.68	1.85	1.83	1.74	1.91	1.90	1.88	2.09	2.01	2.07	2.34

[a] The distance between the fault centre, where pure dip-slip occurs, and the point, were the maximum strike-slip component occurs, is always three-quarters of the fault half length, measured from the fault centre.
[b] Time until the fault has achieved an amount of dip-slip in accordance with the fault scaling law as defined by Schlische et al. (1996). See text for further explanation.

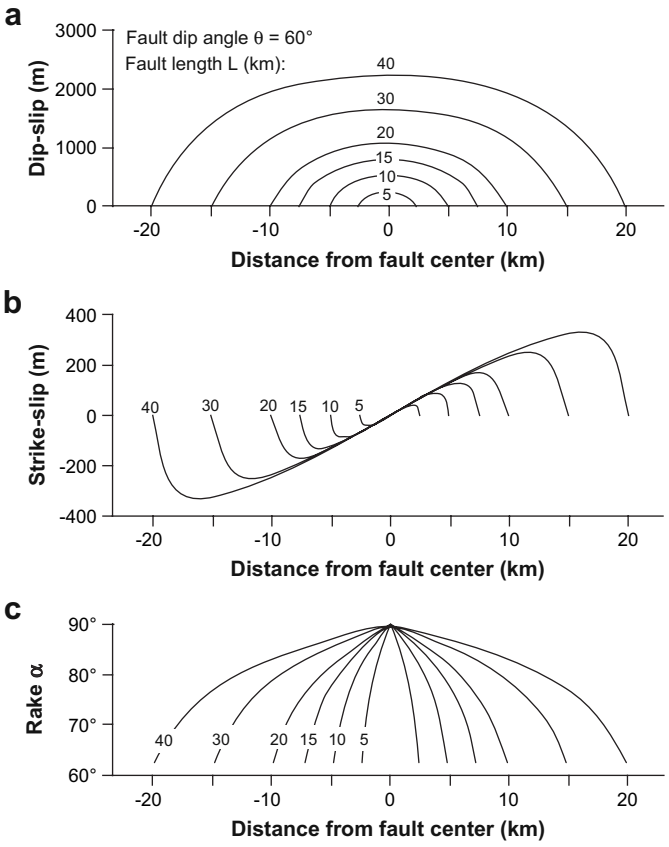

Fig. 3. (a) Dip-slip distributions of six modelled faults dipping 60° when the amount of dip-slip at the centre of each fault corresponds to that anticipated by the scaling law of Schlische et al. (1996) (see Table 1 for amount of dip-slip at fault centre). The lengths of the different faults are indicated as labels on the curves. (b) The distributions of the strike-slip components have the same gradient (within their linear parts). (c) Spatial distribution of the rake α along the faults (Fig. 1b).

distance from the fault centre and to the amount of cumulative dip-slip at the fault centre. Furthermore, the amount of strike-slip at any point along a normal fault (within the range of the near-linear increase) is proportional to the cosine of the fault dip angle and to a power function of the fault length. These relations can be summarized by the following expression, which gives the strike-slip displacement S along a normal fault in dependence on total fault length and dip:

$$S = 2\cos(\theta) l D L^{-1.08} \quad (3)$$

where θ is the fault dip (in degrees), L is the fault length (in metres), l is the distance from the fault centre (in metres), and D is the amount of cumulative dip-slip at the fault centre (in metres). Within the range of the fault parameters examined in this study, the above function yields the amount of strike-slip at any point on the first two-thirds of the distance from the centre of a modelled fault to its tips. The maximum error in the calculation of the strike-slip amount is 16%. This function is not valid in the last one-third of the fault half-length, i.e. near the fault tips where the strike slip distribution is non-linear. To derive the second function, which relates the

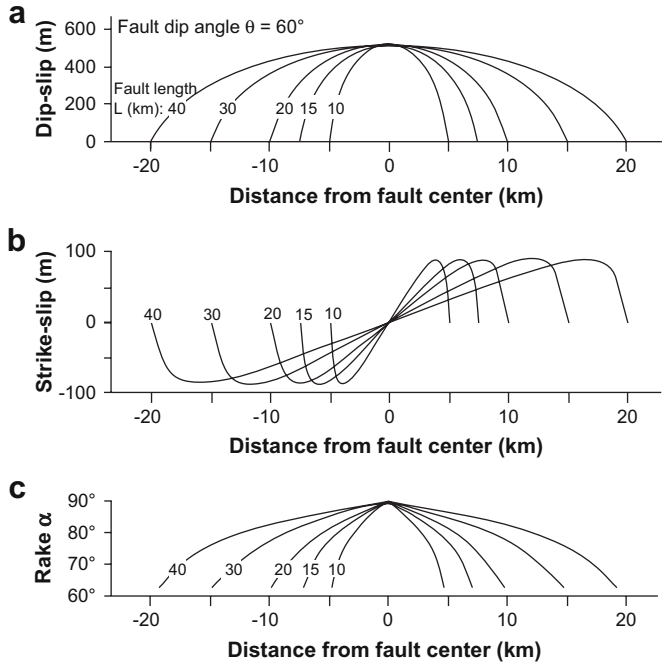

Fig. 4. (a) Dip-slip distributions along 10-, 15-, 20-, 30-, and 40-km-long faults dipping 60° with a maximum dip-slip of 521 m at their centre. (b) Distributions of the strike-slip component. (c) Spatial distribution of the rake α along the faults (Fig. 1b).

rake to fault length and dip, we examined the variation of the slip direction along strike of the fault by analyzing the rake of the slip vector (Fig. 1b). As described previously, the rake is independent of the amount of dip-slip in the fault centre, hence

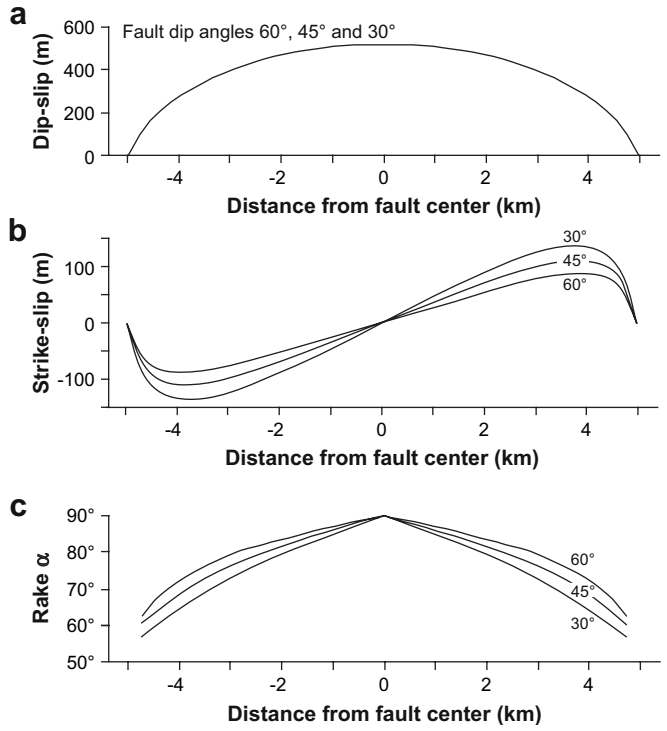

Fig. 5. (a) Dip-slip distribution along three 10-km-long faults with dip angles of 30°, 45° and 60°. (b) Distributions of the strike-slip component. (c) Spatial distribution of the rake α along the faults (Fig. 1b).

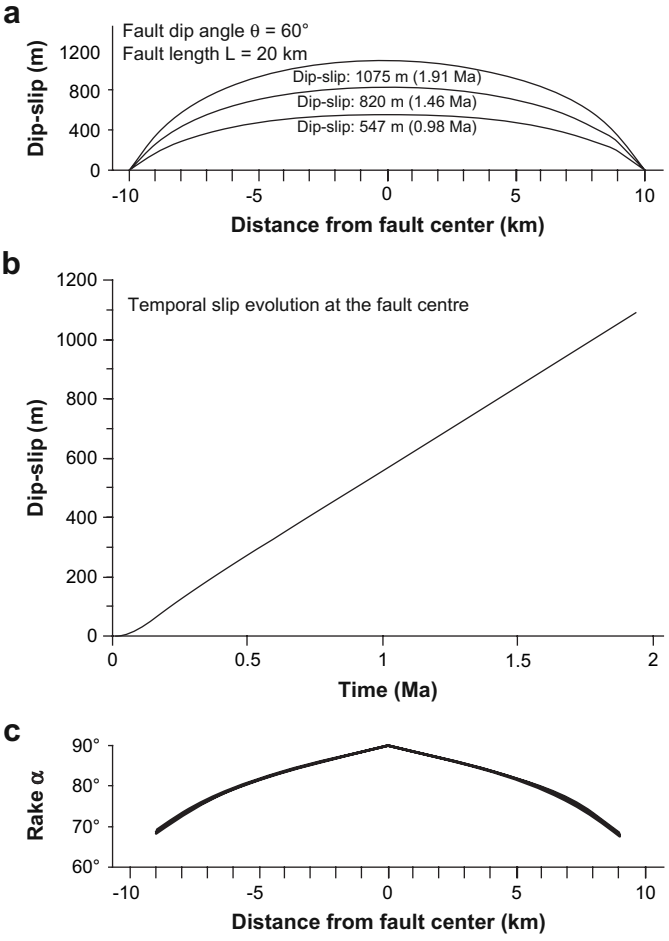

Fig. 6. (a) Dip-slip distributions along a 20-km-long fault model when the dip-slip at the fault centre is 547 m, 820 m and 1075 m, respectively. In case of the 20-km long fault, these amounts of dip-slip are reached after 0.977 Ma, 1.457 Ma and 1.907 Ma, respectively. (b) Temporal evolution of the dip-slip in the fault centre. (c) The distributions of the rake are nearly identical, indicating that the rake of the slip vectors along the fault does not depend on the amount of dip-slip at the fault centre.

D does not appear in the formula. The other geometrical factors control the rake α of the slip vector at a given point along the modelled faults according to the following equation:

$$\alpha = -4000(1/\theta)lL^{-1.08} + 90 \tag{4}$$

where θ is the fault dip (in degrees), L is the fault length (in metres), and l is the distance from the fault centre (in metres). This function gives the rake in degrees at any point along the first two-thirds of the distance from the centre of a modelled fault to its tips with a maximum error of $\pm 3°$. In the last third of the distance between fault centre and tips, i.e. close to the fault tips, the distribution of the rake is non-linear (Fig. 3c) and hence Eq. (4) is not applicable in the vicinity of the fault tips. Toward the fault ends, the rake decreases non-linearly to $\sim 60°$ with the consequence that the slip vectors of the model faults are substantially more oblique than those closer to the fault centre (Fig. 3c).

5. Discussion

The quantitative analysis of our experimental results revealed that the slip direction varies systematically along-strike of the fault and is influenced by fault length and dip. As confirmed by additional experiments, these findings are valid for a range of friction coefficients (0.2–0.8) on the fault plane because this parameter affects mainly the timing of the slip initiation but only to a minor degree the subsequent slip history (not shown in figure; cf. Hampel and Hetzel, 2006). The increasing obliquity of the slip direction near the fault tips can be explained by a local perturbation of the stress field close to the fault tips. According to our numerical models, the trajectories of the minimum principal stress σ_3 are parallel to the extension direction away from the fault but curved toward the hanging wall and footwall centres near the fault tips (Fig. 7). The trajectories of the intermediate principal stress σ_2 are perpendicular to the extension direction away from the fault and deflected towards the fault centre near the fault tips (Fig. 7). The pattern shown in Fig. 7 is representative for the orientation of σ_2 and σ_3 near the fault throughout the upper crust. The oblique orientation of σ_3 in relation to the strike direction of the fault results in oblique slip and local stretching of the hanging wall. This stress orientation and the induced kinematics are in accordance with the along-strike stretching of the hanging wall proposed by Jackson et al. (1982), Ma and Kusznir (1995) and Wu and Bruhn (1994).

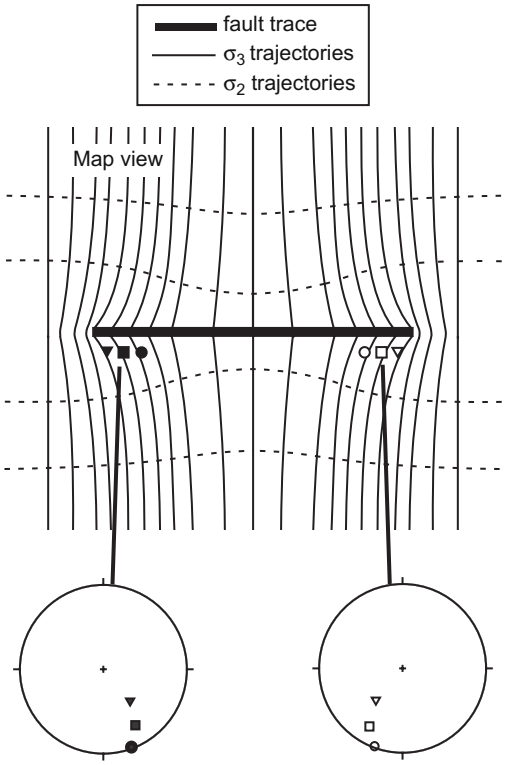

Fig. 7. Schematic sketch showing the orientation of the minimum principal stress σ_3 and intermediate principal stress σ_2 in the vicinity of the fault as derived from our numerical experiments. This is a map view of the σ_2 and σ_3 trajectories at a depth of 7.5 km, i.e. in the middle of the upper crust. Away from the fault the σ_2 trajectories are perpendicular to the extension direction (which is perpendicular to the fault strike). Near the fault tips the σ_2 trajectories are deflected towards the fault centre. The σ_3 trajectories are parallel to the extension direction away from the fault but near the fault tips they point towards the hanging wall centre. Note that this pattern is representative for the orientation of σ_2 and σ_3 near the fault throughout the upper crust. The stereographic plots show the orientation of σ_3 in the hanging wall near the fault tips (at a depth of 7.5 km). The symbols on the map view show the respective locations of the stereographic plots.

In the following, we compare the variation of the slip direction on our model faults with data from two SW-dipping normal faults, the Fucino and Pescasseroli normal faults in the central Apennines (Roberts and Michetti, 2004). We have chosen these faults because they are well investigated and a comprehensive set of slip vector measurements exists for them (Roberts and Michetti, 2004). The Fucino and Pescasseroli faults are 40 km and 20 km long, respectively, and have an average dip angle of $\sim 60^\circ$ at the surface (Roberts and Michetti, 2004; Galadini and Galli, 1999). To allow a direct comparison with our model faults, the slip vectors are shown in map view and stereographic projections (Fig. 8). The map projections of the slip directions show a favourable agreement between the model and natural faults, with the local extension direction converging toward the hanging wall centre both in nature and model. In the stereographic projections, the slip vectors of the modelled and natural faults also agree well, especially along the Fucino fault. The small discrepancies between some of the modelled and measured slip vectors may be caused by the fact that the Fucino and Pescasseroli faults do not have perfectly linear traces and their dip angle is not constant along their trace and at depth (Galadini and Galli, 1999; Cavinato et al., 2002; Roberts and Michetti, 2004) whereas the modelled faults are planar. Furthermore, the slip patterns of the Fucino and Pescasseroli fault are likely affected by the interaction with neighbouring faults, whereas the model fault is isolated.

Another interesting characteristic in the behaviour of the modelled faults is the distribution of lateral slip when the amount of accumulated dip-slip is the one anticipated by fault scaling laws such as the one proposed by Schlische et al. (1996). In this case, the gradient of the lateral slip distribution is nearly constant irrespective of the fault length (see Fig. 3b). This implies that faults with a common dip in nature should display the same amount of lateral slip at the same distance away from their centres. Note that this is valid only for the parts of the faults where the distribution of the lateral slip is linear, i.e. not in the last 1/3 of the distance from the centre of a fault to its tip.

The systematic variation of slip direction along the trace of normal faults has profound implications for studies trying to infer regional palaeostress directions from striations and other kinematic indicators on fault planes. Such studies should only use data from the centre of normal faults to define the regional stress field because kinematic data from areas near the tips of normal faults reflect local stress-field perturbations (e.g. Roberts, 1996) and could misleadingly be interpreted as transtension. Furthermore, different striation sets at the same site along a normal fault may not necessarily indicate a change in the regional stress field. Rather, they may be the result of consecutive and partially overlapping ruptures imposed on the fault by

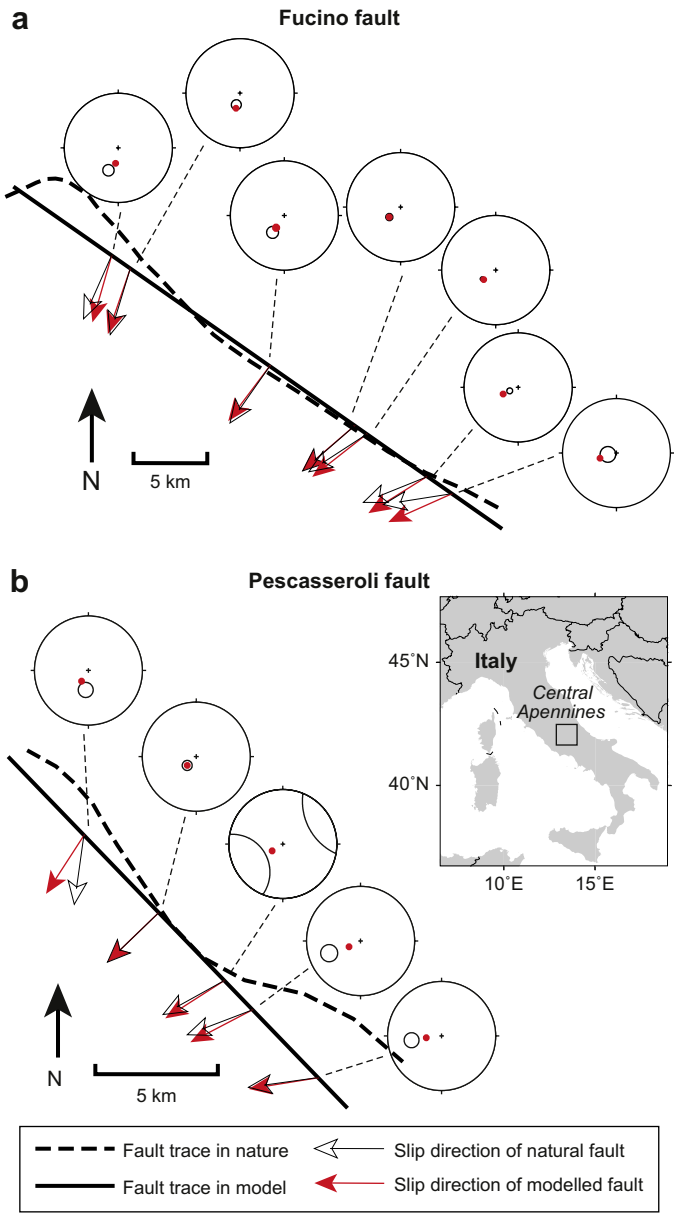

Fig. 8. Comparison between the slip vectors (shown both in map view and stereographic plots) from (a) the Fucino and (b) the Pescasseroli fault in the central Apennines, Italy, and the slip vectors from the model faults of equivalent length. Red arrows depict the slip directions of the model faults, black open arrows the slip direction of the natural fault (after Roberts and Michetti, 2004). In the stereographic projections, the slip vectors of the model faults are shown as red dots and the slip vectors of the Fucino and Pescasseroli faults are shown as the 99% confidence cone of the slip vector (after Roberts and Michetti, 2004).

the same regional stress field (e.g. Roberts and Koukouvelas, 1996). Variations of slip direction along normal faults can also be used as an additional indicator of fault segmentation because areas between fault traces with strongly diverging slip directions probably act as fault segment boundaries (e.g. Roberts and Koukouvelas, 1996). Asymmetric or irregular slip patterns may be the result of fault interaction or may indicate that a persistent fault boundary is hindering fault growth at one of the fault tips.

6. Conclusions

The results of our numerical experiments show that the amount of lateral slip and hence the obliqueness of the slip vector increase from the centre of a normal fault toward its tips. Within two-thirds of the distance between fault centre and tips, the amount of strike-slip at a point along the fault is directly proportional to the distance from the fault centre, the amount of cumulative dip-slip at the fault centre and the cosine of the fault dip. The relation between fault length and strike-slip displacement can be expressed by a simple mathematical expression. Slip vectors along faults are more oblique for shorter or shallower dipping faults but their obliquity is not depending on the amount of dip-slip. The converging motion of the hanging wall can be explained by the local perturbation of the stress field near the fault tips, which causes oblique slip vectors and stretching of the hanging wall. Consequently, slip data from the vicinity of fault centres should be preferred in palaeostress analyses.

Acknowledgements

We thank the referees S. Ellis and A. Ganas for their constructive reviews and R. Hetzel for his critical comments on an earlier version of the manuscript. Funding by the German Research Foundation (DFG) within the framework of an Emmy-Noether fellowship to A.H. (grant HA 3473/2-1) is gratefully acknowledged.

References

Bills, B.G., Currey, D.R., Marshall, G.A., 1994. Viscosity estimates for the crust and upper mantle from patterns of lacustrine shoreline deformation in the eastern Great Basin. Journal of Geophysical Research 99, 22059–22086.

Cavinato, G.P., Carusi, C., Dall' Asta, M., Miccadei, E., Piaccentini, T., 2002. Sedimentary and tectonic evolution of Plio-Pleistocene alluvial and lacustrine deposits of Fucino Basin (central Italy). Sedimentary Geology 148, 29–59.

Cowie, P.A., 1998. A healing-reloading feedback control on the growth rate of seismo-genic faults. Journal of Structural Geology 20, 1075–1087.

Cowie, P.A., Scholz, C.H., 1992a. Growth of faults by accumulation of seismic slip. Journal of Geophysical Research 97, 11085–11095.

Cowie, P.A., Scholz, C.H., 1992b. Physical explanation for the displacement–length relationship of faults using a post-yield fracture mechanics model. Journal of Structural Geology 14, 1133–1148.

Cowie, P.A., Scholz, C.H., 1992c. Displacement-length scaling relationship for faults: data synthesis and discussion. Journal of Structural Geology 14, 1149–1156.

Crone, A.J., Machette, M.N., Bonilla, M.G., Lienkaemper, J.J., Pierce, K.L., Scott, W.F., Bucknam, R.C., 1987. Surface faulting accompanying the Borah Peak earthquake and segmentation of the Lost River fault, central Idaho. Seismological Society of America Bulletin 77, 739–770.

Fjeldskaar, W., 1994. Viscosity and thickness of the asthenosphere detected from the Fennoscandian uplift. Earth and Planetary Science Letters 126, 399–410.

Galadini, F., Galli, P., 1999. The Holocene paleoearthquakes on the 1915 Avezzano earthquake faults (central Italy): implications for active tectonics in the central Italy. Tectonophysics 308, 143–170.

Hampel, A., Hetzel, R., 2006. Response of normal faults to glacial-interglacial fluctuations of ice and water masses on Earth's surface. Journal of Geophysical Research 111, B06406, doi:10.1029/2005JB004124.

Hibbitt, Karlsson, Sorenson, 2006. ABAQUS/Standard, User's Manual, version 6.6. Hibbitt, Karlsson and Sorenson Inc., Pawtucket, RI, USA.

Jackson, J.A., Gagnepain, J., Houseman, G., King, G.C.P., Papadimitriou, P., Soufleris, P., Virieux, J., 1982. Seismicity, normal faulting and the geomorphological development of the Gulf of Corinth (Greece): the Corinth earthquakes of February and March 1981. Earth and Planetary Science Letters 57, 377–397.

Kaufmann, G., Amelung, F., 2000. Reservoir-induced deformation and continental rheology in vicinity of Lake Mead, Nevada. Journal of Geophysical Research 105, 16,341–16,358.

Kim, Y., Sanderson, D.J., 2005. The relationship between displacement and length of faults: a review. Earth-Science Reviews 68, 317–334.

Lambeck, K., Smither, C., Johnston, P., 1998. Sea-level change, glacial rebound and mantle viscosity for northern European Geophysical Journal International 142, 102–144.

Ma, X.Q., Kusznir, N.J., 1995. Coseismic and postseismic subsurface displacements and strains for a dip-slip normal fault in a three-layer elastic-gravitational medium. Journal of Geophysical Research 100, 12813–12828.

Maerten, L., 2000. Variation in slip on intersecting normal faults: Implications for paleostress inversion. Journal of Geophysical Research 105, 25553–25565.

Manighetti, I., King, G.C.P., Gaudemer, Y., Scholz, C., Doubre, C., 2001. Slip accumulation and lateral propagation of active normal faults in Afar. Journal of Geophysical Research 106, 13667–13696.

Michetti, A.M., Ferreli, L., Esposito, E., Porfido, S., Blumetti, A.M., Vittori, E., Serva, L., Roberts, G.P., 2000. Ground effects during the 9 September 1998, Mw = 5.6, Lauria earthquake and the seismic potential of the "aseismic" Pollino region in Southern Italy. Seismological Research Letters 71, 31–46.

Morewood, N.C., Roberts, G.P., 1997. Geometry, kinematics and rates of deformation in a normal fault segment boundary, central Greece. Geophysical Research Letters 24, 3081–3084.

Roberts, G.P., 1996. Variation in fault-slip directions along active and segmented normal fault systems. Journal of Structural Geology 18, 835–845.

Roberts, G.P., 2007. Fault orientation variations along the strike of active normal fault systems in Italy and Greece; implications for predicting the orientations of subseismic-resolution faults in hydrocarbon reservoirs. American Association of Petroleum Geologists Bulletin 91, 1–20.

Roberts, G.P., Ganas, A., 2000. Fault-slip directions in central-southern Greece measured from striated and corrugated fault planes: comparison with focal mechanism and geodetic data. Journal of Geophysical Research 105, 23,443–23,462.

Roberts, G.P., Koukouvelas, I., 1996. Structural and seismological segmentation of the Gulf of Corinth fault system: implication for models of fault growth. Annali di Geophysica 23, 619–649.

Roberts, G.P., Michetti, A.M., 2004. Spatial and temporal variations in growth rates along active normal fault systems: an example from Lazio-Abruzzo, central Italy. Journal of Structural Geology 26, 339–376.

Schlische, R.W., Young, S.S., Ackermann, R.V., Gupta, A., 1996. Geometry and scaling relations of a population of very small rift-related normal faults. Geology 24, 683–686.

Twiss, R.J., Moores, E.M., 1992. Structural Geology. W.H. Freeman, New York.

Walsh, J.J., Watterson, J., 1988. Analysis of the relationship between the displacements and dimensions of faults. Journal of Structural Geology 10, 239–247.

Walsh, J.J., Nicol, A., Childs, C., 2002. An alternative model for the growth of faults. Journal of Structural Geology 24, 1669–1675.

Willemse, E.J.M., Pollard, D.D., Aydin, A., 1996. Three-dimensional analyses of slip distributions on normal fault arrays with consequences for fault scaling. Journal of Structural Geology 18, 295–309.

Wu, D., Bruhn, R.L., 1994. Geometry and kinematics of active normal faults, South Oquirrh mountains, Utah: implication for fault growth. Journal of Structural Geology 16, 1061–1075.